Doped-Iron Oxide Nanocrystals Synthesized by One-Step Aqueous Route for Multi-Imaging Purposes

Yurena Luengo, Manuel A Roldan, Maria Varela, Fernando Herranz,
María del Puerto Morales, and Sabino Veintemillas-Verdaguer

Just Accepted

Doped-Iron Oxide Nanocrystals Synthesized by One-Step Aqueous Route for Multi-Imaging Purposes

Yurena Luengo[a,b]*, Manuel A. Roldan[c], María Varela[d], Fernando Herranz[e], M. Puerto Morales[b], Sabino Veintemillas-Verdaguer[b]

[a]Instituto Madrileño de Estudios Avanzados en Nanociencia, Campus Universitario de Cantoblanco, 28049 Madrid, Spain

[b]Instituto de Ciencia de Materiales de Madrid, CSIC, C/Sor Juana Inés de la Cruz 3, Campus de Cantoblanco, 28049 Madrid, Spain

[c]Eyring Materials Center. Arizona State University (ASU), Tempe AZ 85287 USA

[d]Universidad Complutense de Madrid, Departamento de Fisica de Materiales & Instituto Pluridisciplinar, Madrid 28040, Spain.

[e]Instituto de Química Médica (IQM-CSIC), Juan de la Cierva 3, 28006 Madrid, Spain.

1

ABSTRACT: New doped inorganic nanocrystals (NC) consisting on iron oxide and other metal integrated into the structure have been synthesized in one-step by adapting the oxidant precipitation synthesis route for magnetite. Different metals have been chosen to confer extra and unique properties to the resulting magnetic heteronanostructure: Co and Gd for enhancing transversal and longitudinal relaxivities for Magnetic Resonance Imaging (MRI), and Bi and Au for achieving X-Ray absorption for CT imaging. Apart of that, gold optical properties are interesting for photothermal therapy and iron oxides for magnetic hyperthermia. All metals have been incorporated during the synthesis to the magnetite structure in different ways: by forming a solid solution, by modifying the surface of the NCs or by cocrystallization with the magnetite. The nanostructure formed in each case depends on the ionic radius of the secondary metal ion and the solubility of its hydroxide that control the co-precipitation in the initial steps of the reaction. Magnetic properties and imaging capabilities of the heteronanostructures have been analyzed as a function of the element distribution. Due to the synergistic combination of the different element properties, these magnetic heteronanostructures have great potential for biomedical applications.

INTRODUCTION

The combination of materials with different physical properties in one single structure is a common approach for the creation of novel systems with improved functionalities.[1-3] Among them, the synthesis of doped magnetic nanoparticles (NP) based on iron oxide attracts much attention due to the potential to explore the special functions of two or even more metal elements in biomedicine in a matrix of low toxicity such as the iron oxide.[4-7] Depending on the materials and synthesis method, different structures may appear like solid solutions, doped oxides, core/shell or

2

pudding-like particles, etc. (Figure 1), which determines the properties and applications of the nanomaterials. Interesting metal elements that will be tested in this work are Co, Gd, Bi and Au.

Doping, which involves the intentional addition of appropriate atoms or ions into the host materials, is one effective way of improving the physical/chemical characteristics of the parent materials to obtain desirable properties.[8] Particles of various spinel ferrites can now be routinely prepared using the coprecipitation method by partial or complete replacement of Fe^{2+} ions in magnetite (Fe_3O_4) nanocrystals with other divalent transition metal ions (Co^{2+}, Ni^{2+}, Mn^{2+}) [4, 9-11] or with lanthanide ions (Gd^{3+}, Eu^{3+}, Dy^{3+}). [7, 12-16]

In the case of Co, it is incorporated by partial or complete replacement of Fe^{2+} ions in magnetite (Fe_3O_4) nanocrystals.[4, 9, 17-18] The complete replacement of Fe^{2+} gives rise to cobalt ferrite that exhibits a cubic spinel structure with a ferromagnetic nature, [19-20] along with interesting electronic, magnetic, optic and catalytic properties.[21-24]
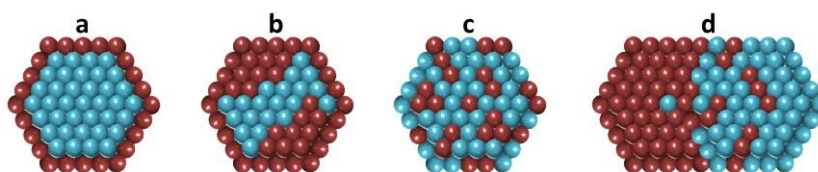
Figure 1. Schematics showing different types of doped nanoparticles: (a) core/shell, (b) phase-segregated, (c) solid solution and (d) coalesced nanoparticles.[3]

Magnetic NPs engineered by Gd doping have also attracted considerable attention due to their wide applications in biology, catalysis and solar cells,[7-8, 12] showing intriguing properties based on its strong paramagnetic character coming from its seven unpaired 4f electrons (Gd^{3+}). This property can be advantageously exploited for MRI[25-26] producing T_1-T_2 dual modal magnetic resonance imaging (MRI) contrast agents.[27-33] Gadolinium-based agents still have relatively low sensitivity, so a high dose of contrast agents should be used. In addition, free gadolinium ions

3

leached from the complexes can have toxic side effects such as nephrogenic systemic fibrosis (NSF).[34] Moreover, most gadolinium complexes are designed to have a very short circulation time, which precludes high-resolution and/or targeted MRI for longer times after injection.[35] The advantage of using dual nanoparticles for MRI is that they have a longer half-life in blood, so they allow not only to detect a lesion but also to monitor the evolution over time of a given treatment, greatly improving the traceability of the nanoparticles in the organism.[36] In addition, the presence of superparamagnetic nanoparticles of iron oxide allows the application of a local treatment of magnetic hyperthermia, so it would be a theranostic material, since it would not only allow the detection of a tumor but also its treatment. The magnetic hyperthermia properties of gadolinium-doped magnetite have received much less attention.[37-38]

Other two interesting nanoparticles proposed as X-ray contrast agents are bismuth and gold nanoparticles, which could overcome some significant limitations of iodine-based agents. In both cases, nanoparticles are expected to be cleared from the blood circulating system more slowly than iodine agents, permitting imaging for longer time. Previous works described new magnetite/bismuth oxide core/shell magnetic nanoparticles with great potential in cancer therapy. Such particles combine the ability to image a specific tumor area by MRI and tomography (CT), the ability to target it under the influence of a magnetic field and the treatment by magnetothermia.[39-41]

In the case of gold, we expect higher X-ray absorptivity than iodine with less bone and tissue interference achieving better CT contrast with lower X-ray dose. Ideally, gold nanoshells on magnetic nanoparticles should be thin enough to induce minimal alteration of the magnetic properties of the magnetite core. Gold-coated NPs can provide a number of additional advantages, such as near-infrared (NIR) absorption, photon scattering, and the preservation of the core

4

magnetic properties.[42] Moreover, due to the absorption of NlR of the nanoshell its illumination by a laser also generates heat. This property helps gold shell to act as a potent material for optical hyperthermia also.[43-45] Another class of gold-magnetite composites has also been reported involving the attachment of discrete gold nanoparticles onto magnetite without forming a full coating.[46-47] Such composites may be useful in applications such as protein separation, optical imaging or catalysis, where a full coating is not necessarily required and has the advantage of having not only the gold surface but also the iron oxide surface partially available for further functionalization.

In this work we propose a single step green chemistry process based on the oxidative precipitation method[39-40] for the preparation of doped magnetic nanostructures based on iron oxide and containing Co, Gd, Bi and Au as secondary metal component. We analyzed the final structure of the bimetallic magnetic nanocrystals to localize, quantify and determine the distribution of the metals, i.e. if they are forming a solid solution, core/shell or pudding-like particles. Finally, we studied the magnetic and optical properties as a function of the structure of the nanoparticle and the possible use of these materials for imaging applications such as MRI or CT contrast agents.

EXPERIMENTAL SECTION

Doped magnetic nanocrystals were obtained by ageing at 90 ºC the amorphous hydroxide formed by addition of acidic solutions of $FeSO_4$ and variable amounts of $Co(NO_3)_2$, $Bi(NO_3)_3$, $HAuCl_4$, or $Gd(NO_3)_3$ to a NaOH solution in presence of sodium nitrate that actuates as mild oxidant. The process was carried using hydroalcoholic solution 25% w/w as solvent and in a glove box under nitrogen. Previous works explored the effect on the particle size of the [OH⁻] excess[48] for the pure iron oxide case and the addition of bismuth to the reaction.[39] In all the cases the iron (II) and nitrate concentrations were 0.2 M. The base excess was computed considering the formation of ferrous

5

and the secondary metal hydroxides as well as the base needed to neutralize the acid used in the

dissolution of the metallic salts (usually 0.01M H_2SO_4) (Equation 1).

$$[OH^-]_{EXCESS} = [NaOH] - 2[Fe^{2+}] - m[M^{+m}] - n[H_nA] - p[H_pM] \quad (1)$$

where n is 1 or 2 depending on the monoprotic or diprotic character of the acid used to dissolve

the iron salt, m is the oxidation state of the metal used and p is the number of acid protons of the

precursor salt (case of $HAuCl_4$ were p=1). For each case the [NaOH] was adjusted to keep

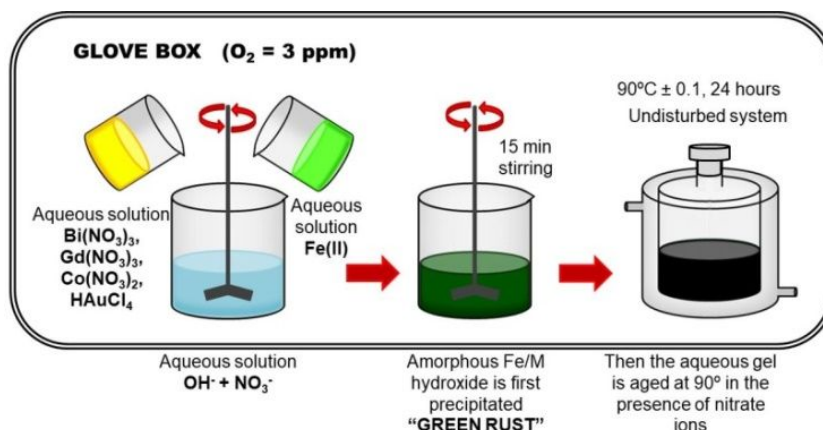constant the $[OH^-]_{EXCESS}$=0.02.

Figure 2. Scheme of the experimental synthesis of doped magnetic nanocrystals by oxidative precipitation.

The mixing of the metal solution and the alkaline-oxidation was carried out under stirring, obtaining a final volume of 250 ml. The precipitation of the green rust was completed by overhead stirring for 15 min. After this time, the reaction intermediate was aged at 90 ºC for 24 h without agitation to obtain the doped magnetic nanocrystals (Figure 2). Ageing time was fixed at 24 h in order to reach conditions close to the equilibrium. Finally the system was left to cool and the nanocrystals were separated by magnetic decantation and washed with distilled water outside the glove box.

6

In most cases the secondary metal salt could be dissolved in 25 ml of 0.01 M HCl, H_2SO_4, or HNO$_3$ depending of the salt employed. However, Bismuth Bi(NO$_3$)$_3$ was dissolved in 25 ml of 1.73 M HNO$_3$ due to the easy hydrolysis of Bi^{3+} and HAuCl$_4$ was dissolved in 25 ml of water, separately to prevent oxidation of the iron (II) sulphate (Figure 2). Previous experiments demonstrated that lower polydispersity was obtained when the two metal solutions were added simultaneously to the NaOH+NaNO$_3$ solution. However, HAuCl$_4$ was added shortly after the precipitation of the green rust, to favor the hydrolysis of Au^{3+} and limit its reduction to non-reactive Au^0 by ionic Fe^{2+}.

The samples were studied by X-ray powder diffraction performed in a Bruker D8 Advance powder diffractometer using Cu Kα radiation with an energy-discriminator (Sol-X) detector. The patterns were collected between 10° and 70° in 2θ. The XRD spectra were indexed to an inverse spinel structure. The average crystallite size of the magnetic core was calculated by Scherrer's equation using the half width of the (311) X-ray diffraction peak of magnetite using the utilities of the automatic powder diffraction computer program (APD) from Phillips. The error in the crystallite sizes obtained by use of the Scherrer's equation is ±0.1 nm and is related to the instrumental line width of the diffractometer (Δ2θ = 0.11°).

Particle size and shape were determined by transmission electron microscopy (TEM) using a 200 keV JEOL-2000 FXII microscope. TEM samples were prepared by placing one drop of a dilute suspension of maghemite nanoparticles in water on a copper grid covered with a perforated carbon film and allowing the solvent to evaporate slowly at room temperature. The particle size distribution was evaluated by measuring the largest internal dimension of at least 300 particles. Afterward, the distribution was fitted to a log normal distribution by obtaining the mean size and the polydispersity index (PDI) defined as the quotient between the standard deviation (σ) and the

7

mean size. Atomic resolution scanning TEM (STEM) images and high angle annular dark field (HAADF) images were acquired in a Nion UltraSTEM200 equipped with a spherical aberration fifth-order corrector and a Gatan Enfinium electron energy-loss spectrometer (EELS). A Nion UltraSTEM100 operated at 60 kV and equipped with a Nion aberration corrector and a Gatan Enfina spectrometer was also used.

The magnetic characterization of the powders was carried out using a vibrating sample magnetometer MagLabVSM (Oxford Instrument) with a maximum field of 50 kOe. Coercive field and saturation magnetization values were obtained from the hysteresis loops recorded at room temperature (250 K) after applying a magnetic field of ±5 T. We evaluated the saturation magnetization values (Ms) expressed in Am^2/Kg_{Fe} by extrapolation to infinite field using the linear M versus 1/H plot.

Optical properties of the gold doped magnetic nanoparticles were measured in water dispersion (0.1 mg_{Fe}/mL) with a Varian Cary Bio UV-Visible spectrophotometer over the wavelength range from 450 to 700 nm using a 1 mm wide quartz cuvette.

In order to evaluate the efficiency of the suspensions as contrast agents for MRI, measurements of the relaxation times of water protons (both T_1 and T_2) in the presence of magnetic nanoparticles were carried out in a time-domain NMR benchtop system MINISPEC MQ60 (Bruker) at 37º and 1.5 T using standard methods. The relaxivities r_1 and r_2 ($s^{-1} \cdot mM_{Fe}^{-1}$) were obtained from the measured longitudinal and transversal relaxation times T_1 and T_2 of gelated (agar 0.5%) dispersions of samples at concentrations below 1 mM_{Fe} from the linear plot of $1/T_1$ and $1/T_2$ as a function of the concentration.

CT phantom imaging was performed with a nanoPET/CT small-animal imaging system (Mediso Medical Imaging Systems, Budapest, Hungary). MicroCT was performed for attenuation

8

correction. Images were reconstructed using a Tera-Tomo 3D iterative algorithm. Acquisition was performed with a helical scan at 65 Kv. Acquisition and reconstruction was performed with proprietary Nucline software (Mediso, Budapest, Hungary). Image analysis was performed using Horos software (Horos is a free and open source code software (FOSS) program that is distributed free of charge under the LGPL license at Horosproject.org and sponsored by Nimble Co LLC d/b/a Purview in Annapolis, MD USA).

Heating capacities of Co and Gd doped nanocrystals in colloidal form were measured using the commercial ac field applicator DM100 by nanoscale Biomagnetics© in the frequency range from 416 to 828 kHz and magnetic fields (H_0) of 20 to 24 kA/m at an iron concentration of 5 mg/ml. Experiments were carried out within a thermally-insulated working space of about 1 cm^3, using a closed container of 0.5 ml volume conditioned for measurements in the liquid phase. The temperature of the colloids was measured using an optic fiber sensor incorporated in the equipment and registered using a computer. Prior to turning the magnetic field on, the sample temperature was recorded for about 30 s to ensure thermal stability and to have a baseline for the calculation of the specific absorption rate (SAR). As the field was turned on, the temperature increase was measured during 300 s. By performing a linear fit of the data (temperature versus time) in the initial time interval, the slope $\Delta T/\Delta t$ can be obtained in the first few seconds after turning the magnetic field on. The time range was selected such as when the slope is maximum, typically during the first 30 s. Then, SAR values (W/g$_{Fe}$) can be calculated using Equation 2 where C_{liq} is the specific heat capacity of water (4.185 J/g·K) and c_{Fe} is the Fe weight concentration in the colloid.

$$SAR = \left(\frac{C_{liq}}{c_{Fe}}\right)\left(\frac{\Delta T}{\Delta t}\right) \tag{2}$$

RESULTS AND DISCUSSION

9

Composition. The doped magnetic nanocrystals obtained in this work present X-Ray diffraction

patterns that correspond to a inverse spinel structure similar to magnetite (Figure 3). Additional

peaks corresponding to the secondary M_2O_3 oxide (M=secondary metal) or Au nanocrystals

appeared for atomic ratios greater than 5 %$_{at}$. Only in the case of 20 %$_{at}$ cobalt, we observed a shift

of the peaks consistent with the formation of a solid solution $Co_xFe_{3-x}O_4$.

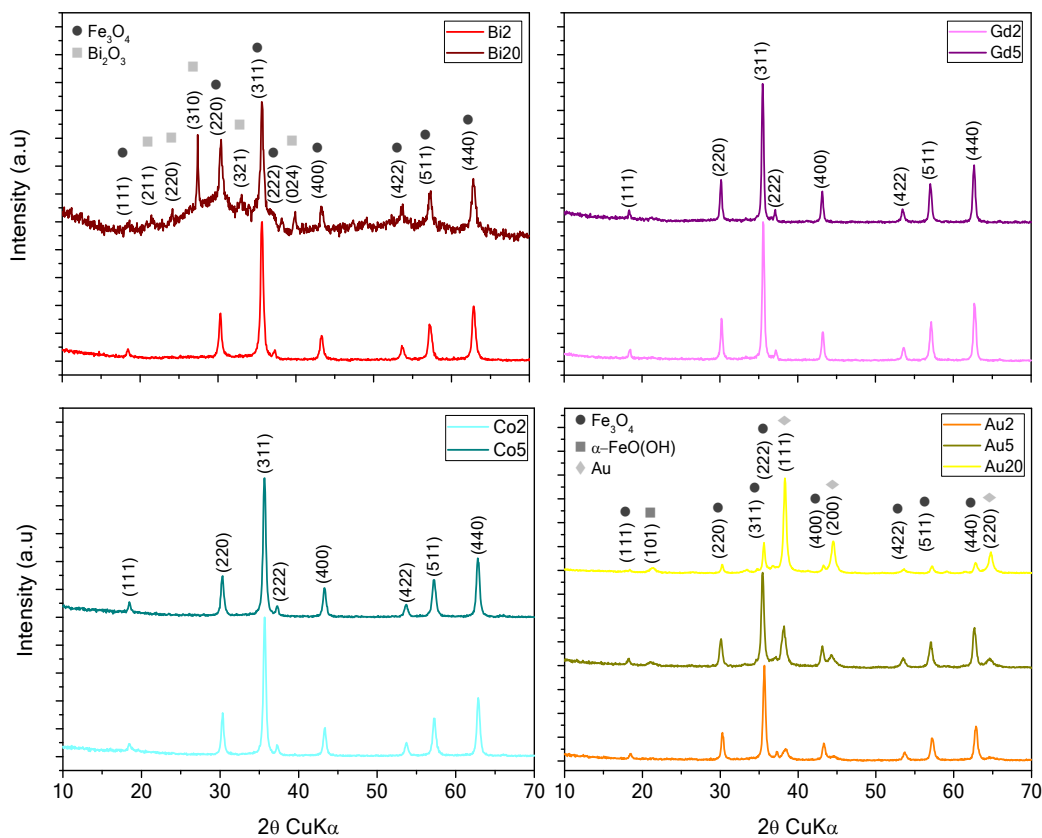**Figure 3.** X-ray diffraction patterns of doped magnetite nanocrystals with different secondary

metal content $((M/Fe)_{at}x100)$.

The proportion of secondary metals follows closely the preexistent in the reactant mixture as

determined by ICP (Table 1). This result indicates that both iron and secondary metal coprecipitate

during the reaction process. The differences between the measured and the estimated values in the

case of gold nanocrystals are probably due to the loss of not bonded gold during the washing process.

TEM micrographs of different doped magnetic nanocrystals prepared with atomic percentages of secondary metal between 2 and 20 %$_{at}$ show nanoparticles with sizes ranging between 26 and 51 nm in diameter (Figure 4). Size distributions are included in the SI (Figure S1).
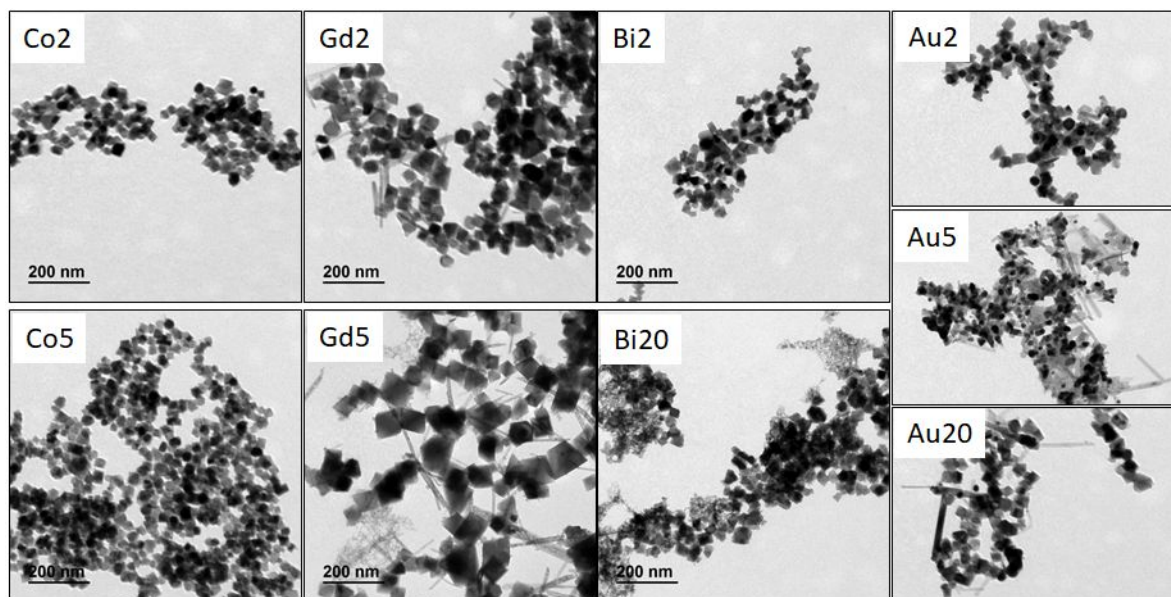

Figure 4. TEM micrographs of doped magnetite nanocrystals with different secondary metal content.

Table 1. Composition, particle (TEM) and crystal (XRD) size and magnetic properties (M_S=Saturation magnetization and H_C=Coercivity) for the doped magnetic nanocrystals obtained by varying the secondary metal concentration. [M] is referred to Bi, Gd, Co and Au, respectively. %M_0 and %M_{exp} are given in atomic ratio ((M/Fe)$_{at}$ x 100). M_0 refers to the initial ratio and M_{exp} to the analytical ratio obtained in the final product measured by ICP-OES.

11

Id.	%$_{at}$ M$_0$	%$_{at}$ M$_{exp}$	TEM Size (nm)/PDI	XRD Size (nm)	M$_S$ (Am^2/kg$_{Fe}$)	H$_c$ (kA/m)
Fe$_2$O$_3$	-	-	21/0.23	21.4	78	7
Bi2	2	2.2	29/0.36	28.6	119	8
Bi20	20	19.0	19/0.60	19.8	76	2
Gd2	2	1.6	42/0.31	40.9	123	9
Gd5	5	4.0	51/0.40	50.6	119	10
Co2	2	2.2	30/0.27	28.6	122	33
Co5	5	5.0	26/0.24	25.4	126	78
Au2	2	2.3	34/0.34	34.2	113	8
Au5	5	4.3	31/0.39	29.0	112	8
Au20	20	16.8	31/0.46	29.1	58	9

Table 1 also summarize the effect of varying the secondary metal concentration ((M/Fe)$_{at}$·100) on particle size. In general, particle size decreases as the secondary metal concentration increases except for the case of Gd, indicating that Gd is not interfering in the iron oxide nucleation and growth, and most probably is forming a shell on the iron oxide nanoparticle as previously observed by other synthesis methods.[49] Crystal size calculated by XRD from the width of the (311) peak agrees well with the TEM size, which strongly suggests that each particle is a single crystal.

Element distribution. Figure 5 shows HAADF images of 2 %$_{at}$ Bi, Gd and Co samples. In this figure the heavier Bi and Gd atoms (not distinguishable under ordinary TEM observation) appear brighter than Fe atoms. The shell that concentrates most of the Bi or Gd atoms appears discontinuous with the Bi and Gd atoms distributed as isolated surface atoms or in small clusters. In the case of Bi, the clusters were presumably bismuth oxide, since additional peaks corresponding to Bi$_2$O$_3$ are observed in Bi20 X-Ray pattern (Figure 3). In contrast to that, cores

12

appear as well-ordered magnetite crystals (the crystalline planes and the absence of defects are clearly observed in high-resolution micrographs (Figure 5)).

STEM-EELS measurements were also performed and the spectra provide an accurate representation of the local composition of the material. This spatially-resolved compositional analysis is essential in determining the location of Gd and Co in the nanocrystals. The EEL spectrum (Figure 5) confirms the presence of Gd and Co in the samples; the former is specifically distributed on the surface of the nanocrystals while the latter is uniformly distributed inside the nanocrystal forming a solid solution.
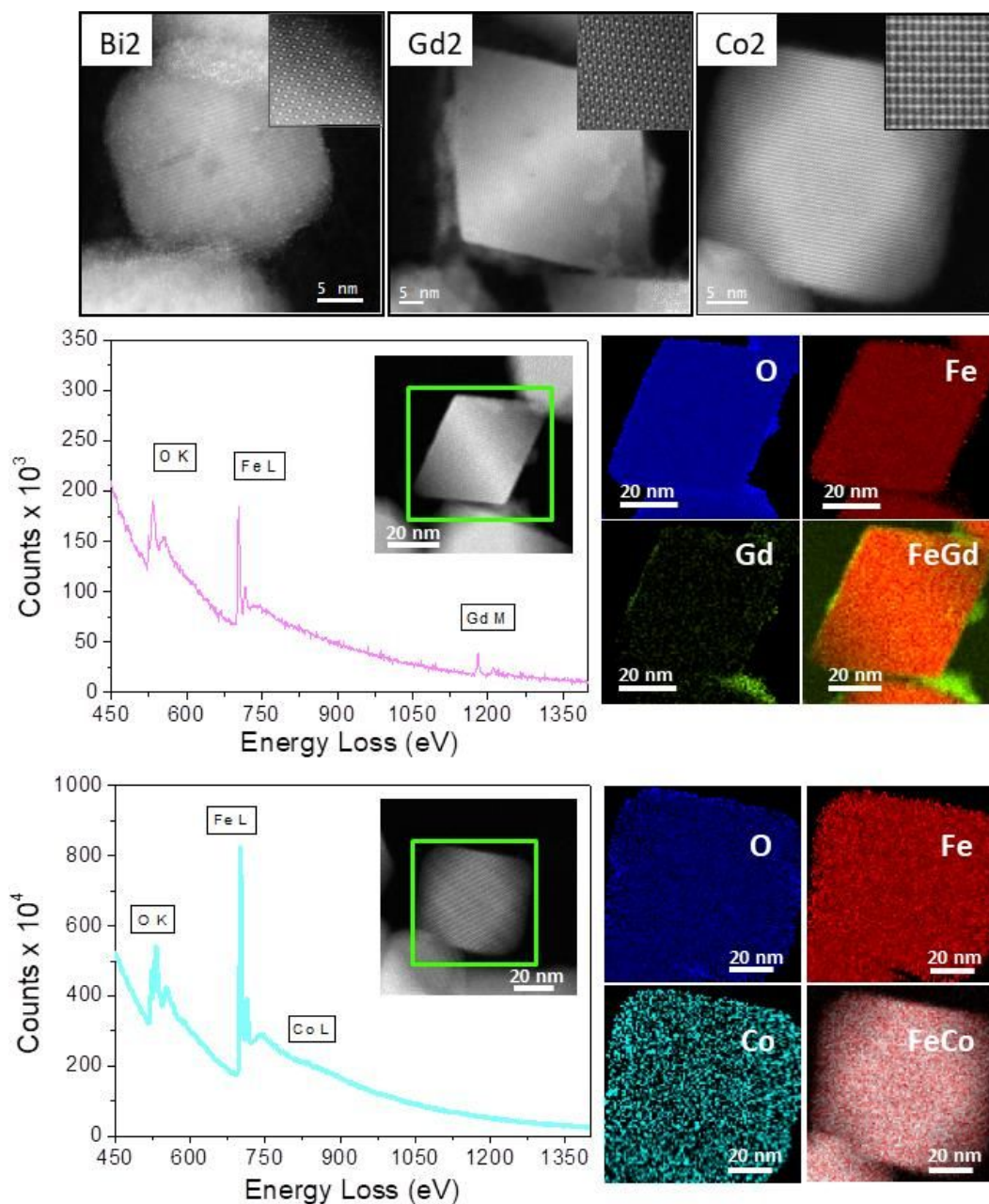
13

Figure 5. HAADF images of 2%$_{at}$ Bi, Gd and Co nanocrystals (iron atoms or crystalline planes are observed in the insets) along with EEL spectrum and elemental distributions obtained from EEL spectrum images of 2%$_{at}$ Gd and 2%$_{at}$ Co nanocrystals (O: blue, Fe: red, Gd: green, Co: cyan).

Iron oxide-gold nanocrystals present irregular pudding-like morphologies in which gold nanoparticles having more contrast. This microstructure indicates that gold shows no affinity

towards the magnetite nanoparticles, but simply disturb their growth and remain attached to their surfaces (Figure 6). The crystal sizes calculated from the gold peak (111) are 14 nm, 18 nm and 27 nm for the samples Au2, Au5 and Au20, respectively while iron oxide nanoparticles have an average size of around 30 nm.
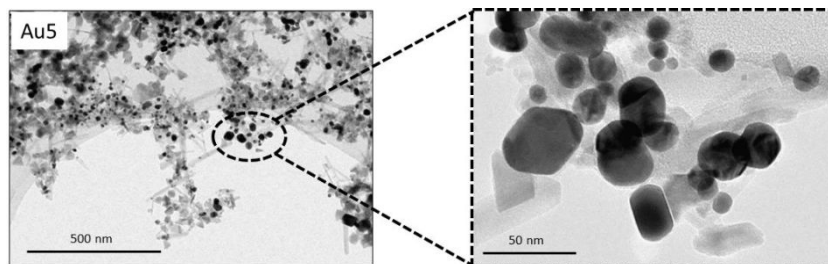
Figure 6. TEM images of Au5 sample at low and high magnification.

Formation mechanism. The co-crystallization of Bi, Gd, Co, and Au with magnetite under the conditions employed in the present work has resulted in: (1) The formation of a core-shell nanostructure, as it is the case for Bi and Gd, (2) the formation of a solid solution as in the case of Co, and (3) the decoration of the surfaces or mixture of particles of different nature, that is the case of Au. In order to understand these differences, we consider the differences in ionic radius and reactivity of these ions.

In the Table 2 and Figure 7 the physicochemical characteristics of all the ions used in this study are summarized. The similitude of the ionic radius of Fe^{2+} and Co^{2+} justifies the formation of a solid solution. Other cations present much larger ionic radius, like Gd^{3+} 0.93 Å, Bi^{3+} 0.96 Å and Au^{3+} 0.85 Å that limit the possibility of the solid solutions formation. The high positive reduction potential of Au^{3+} (much bigger than nitrate) makes it the most powerful oxidant in the media with the immediate production of metal gold nanoparticles, that due to its low reactivity could only decorate the surface of magnetite or form a particle apart.

15

Table 2. Ionic radius, solubility product of the hydroxide and reduction potential of the metal cations involved in the synthesis of doped magnetic nanocrystals.[50-51]

	Fe	Bi	Gd	Co	Au
r_{M3+} (Å)	0.64	0.96	0.93	0.63	0.85
r_{M2+} (Å)	0.74			0.72	
Kps $M(OH)_3$	$6.3 \cdot 10^{-38}$	$3.2 \cdot 10^{-40}$	$8.9 \cdot 10^{-23}$	$4 \cdot 10^{-45}$	$1 \cdot 10^{-53}$
Kps $M(OH)_2$	$7.9 \cdot 10^{-15}$			$2.5 \cdot 10^{-16}$	
Reduction Potential (V)	0.77 (+3,+2)	0.308 (+3,0) 0.2 (+3,+1)	-2.28 (+3,0)	-0.28 (+2,0)	1.498 (+3,0)
$NO_3^- + H_2O + 2e^- = NO_2^- + 2OH^-$ $E^o = 0.01$ V					

The solubility product values were obtained from http://www.chemeddl.org/services/moodle/media/QBank/GenChem/Tables/KspTable.htm

In the case of bismuth, gadolinium and cobalt ions, they effectively co-precipitate as hydroxides with $Fe(OH)_2$ and evolve parallel towards the final product, forming either a core/shell nanoparticle as it is the case of Bi and Gd, or a solid solution in the case of Co, that seems to not alter its oxidation state during the process. Since Co^{2+} and Fe^{2+} form hydroxides with similar solubility product constants, an exchange of Co^{2+} for Fe^{2+} in the green rust (intermediate reaction) is expected to take place.[52] Consequently, very homogeneous nanocrystals in size and shape were obtained.

On the other hand, differences in the quality of the coating between Bi and Gd seem related to the match of the solubility product of the metal hydroxide with the Fe (III). In this sense, bismuth with better match forms more homogeneous coatings than gadolinium (Figure 5). More subtle differences come from the hydrolysis behavior of the different metals represented in the Figure 7. Again, bismuth behaves differently than the rest of the ions due to his unique ability to form

16

positive species BiO^+ in strong alkaline conditions. This could be relevant if we consider that all colloidal forms of iron hydroxides present a negative surface neat charge at pH>9. Bismuth cations with positive charge will be attracted similarly to $FeOH^+$ to the growing magnetite nuclei, altering their growth rate and reducing the final nanoparticle size as observed in this study and previously[39] at low Fe concentrations. The strong hydrolysis and extremely low solubility of the hydroxides are responsible for the final nanostructure consisting of a bismuth layer on the surface of the magnetite core. From the HAADF images, it can be observed that bismuth atoms are not homogeneously distributed on the particle surface. Similar samples were studied by X-ray absorption spectroscopy (XAS) and revealed that the Bi atoms do not form a well-defined Bi oxide structure and that the bismuth shell consists in clusters $[BiO_{6-x}(OH)_x]$ bonded by multiple hydroxyl bridges to the magnetic core.[40] However, when increasing the proportion of Bi up to 20% we get more polydispersed particles and we do not achieve such a drastic reduction in particle size as previously observed.[39]
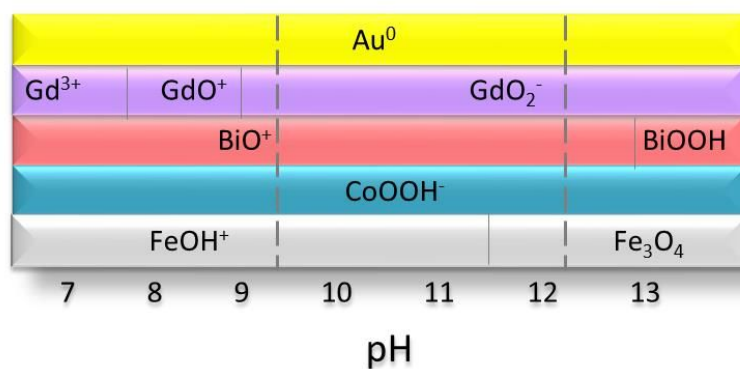

Figure 7. Stable form of the metal ions in solution as a function of pH at 10^{-10} M and 298 K. The two vertical lines mark the pH range of the magnetite crystallization.[53]

In the case of gadolinium, it seems that this element has been left out of the magnetite structure, decorating the surface of the nanoparticles as in the case of Bi, which is in accordance with the

17

results obtained by Li et al.[49] However, it has been reported that gadolinium may be incorporated into the structure of magnetite with no significant structural modifications but decreasing the magnetic moment.[8, 38, 54-55] Our results do not support this incorporation.

Gold decorated magnetite nanoparticles have up to our knowledge not prepared previously in one step. Most of the studies were focused in the obtaining of core-shell nanostructures of iron oxide/gold involving at least two steps (the synthesis of iron nanoparticles and subsequent gold coating) which could adversely affect the yield and the reproducibility of the process.[42, 46-47, 56-57] However, the achieved association could be viewed more as an intimate mixture than as a core-shell nanostructure.

In the case of magnetite samples prepared in the presence of Au^{3+} and Gd^{3+}, goethite (a pure Fe(III) phase) appears as secondary phase (figure S2). It is commonly accepted that the presence of goethite in the synthesis of magnetite starting from a Fe(II) precursor is related to a fast oxidation, taking into account that prior oxidation, dehydroxylation of iron complexes should occur.[58] In the preparation of pure magnetite by oxidative precipitation the appearance of goethite as secondary phase is related to the presence of trace amounts of oxygen that accelerates the oxidation of Fe^{2+}. In the case of the doped samples, the presence of goethite was due to the oxidant cation Au^{3+} substituting the oxygen. Gadolinium ion is not oxidant and its relation with the formation of goethite is unclear.

Magnetic properties. In Figure 8 are plotted the magnetic parameters at room temperature for the doped magnetic nanoparticles (hollow symbols) and pure magnetite nanoparticles for comparison (dense symbols). In general, the saturation magnetization of the doped nanoparticles is similar to the magnetite nanoparticles of similar size except for heavily enriched NPs in the secondary metal (Bi20 and Au10). Saturation magnetization increases with particle size from 110

18

Am^2/Kg_{Fe} to 125 Am^2/Kg_{Fe} for 20 nm and 90 nm particles, respectively. However, the coercivities are higher for the doped NPs than those for pure magnetite, especially for Co5. The coercivities of nanoparticles containing Gd, Bi and Au are independent of the secondary metal ratio but dependent on the particle size. It means that the presence of the secondary metal affects the magnetic anisotropy of the particles increasing it, either because of the increase of the crystalline anisotropy (Co) or because of the reduction of surface defects (Bi, Gd).
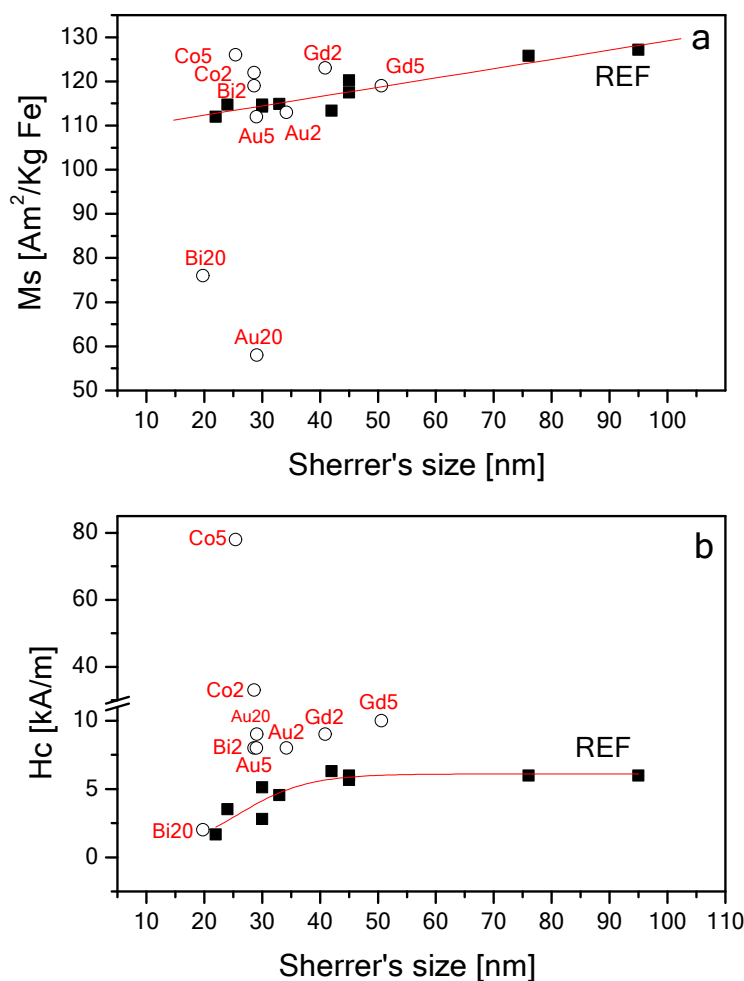
Figure 8. Comparison among the saturation magnetization (a) and coercivities (b) of doped nanocrystals (hollow symbols) and pure magnetite nanocrystals obtained by the same method (dense symbols) at room temperature.

19

In the case of samples containing Co, saturation magnetization values are below the saturation magnetization of bulk cobalt ferrite but its value increases with cobalt content in spite of some reduction in particle size. The obtained results are in accordance with previous observations on Co doped magnetite nanoparticles where M_S shows a maximum together with the magnetic anisotropy at x=0.6 for $Co_xFe_{3-x}O_4$.[59] This maximum was not observed by Sathya and coworkers[9] that reported a continuous decrease of M_S as the cobalt proportion increased from x=0.1 to x=1. This has been interpreted due to the Co^{2+} ions, being smaller that the Fe^{2+} ions, tend to occupy both the octahedral sites and the smaller tetrahedral sites, breaking the antiferromagnetic ordering among the Fe^{3+} ions.[9] Our samples with Co exhibit a coercivity increase from 33 kA/m up to 78 kA/m with the cobalt content in accordance with the reported increase of this magnitude from x=0.1 to x=0.5 at which the maximum H_C value is obtained.[9, 59-60]

Imaging capabilities. Doped magnetic NCs containing Co and Gd have been evaluated as MRI contrast agents. Study of the relaxometric properties was carried out by measuring the proton relaxation times (T_1 and T_2) at various concentrations of iron and calculating relaxivity values (r_1 and r_2). In Figure 9, it can be observed that doped nanocrystals present maximum r_1 and r_2 for 30 nm core size. Larger nanocrystals showed a decrease of both r_1 and r_2 values. In all samples r_2 values, which are responsible for the negative contrast of the nanoparticles, are of the same order or greater than those reported for commercial contrast agents and other superparamagnetic iron oxide nanocrystals synthesized by the decomposition method.[61-62]

The X-ray attenuation was measured on phantoms of different concentrations of Bi20 in water and compared with standard iodine-based contrast (Figure 8). As expected, the Bi20 sample presents higher opacity than Xenetix® measured by the slope of the linear plot of the CT numbers (HU) against the concentration, as previously reported.[41]
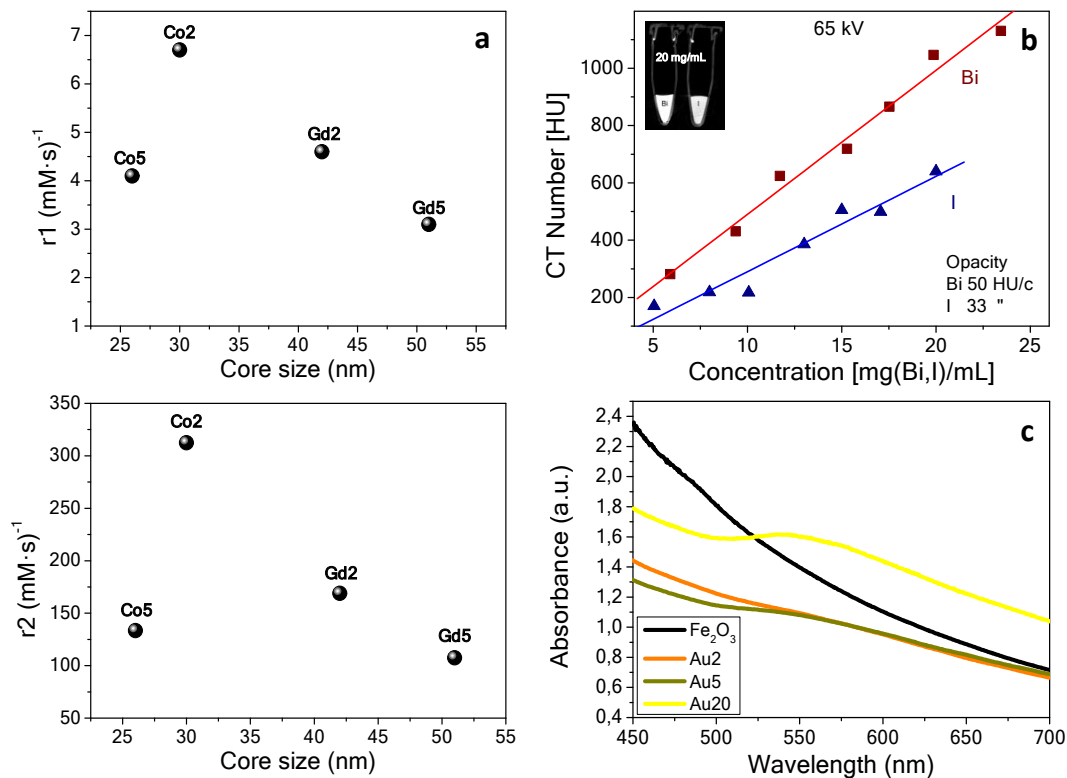
20

Figure 9. a) NMR relaxivities, r_1 and r_2, vs. particle size for Co and Gd doped nanocrystals. b) X-ray attenuation of sample Bi20 as a function of the bismuth concentration at 65 kV in CT numbers (HU), HU=1,000(μ-μw)/μw, where μ and μw are the linear absorption coefficients of the sample and water, respectively. The iodine-based commercial sample Xenetix 350® (Gerbet, France) was shown for comparison. c) UV-Vis absorption spectra comparing pure magnetite and samples containing different amount of gold.

Finally, we present the UV-Visible absorption spectra of Fe_3O_4/Au nanoparticles in Figure 9. Samples with Au content above 5% showed a broad band corresponding to the surface plasmon resonance (SP) of the gold particles at around 540 nm. This wavelength corresponds to pure gold particles of 60 nm, however since the gold particles present in our samples are much smaller we assumed that this red shift is due to the interaction between gold and magnetite nanoparticles. Similar quenching effect has been previously observed for luminescent and magnetic NPs.[63-64]

21

Heating capacity. The heating power of Co and Gd nanocrystals is presented in Figure 10. SAR values are obtained by fitting the experimental heating curves and normalizing to the iron mass (W/g_{Fe}). From these results it can be observed that in all cases, the highest SAR value is obtained when the samples are measured at 710 kHz and 24 kA/m ($H_0 \cdot f = 1.7 \cdot 10^{10}$ A/m·s, close to the recommended value $5 \cdot 10^9$ A/m·s). Samples doped with Co present SAR values lower than samples doped with Gd, which could be related to the larger anisotropy of the Co samples (Hc=33 and 78 kA/m for Co2 and Co5, respectively) and the low amplitude of the magnetic field used in this experiment. These results support the fact that Co is incorporated in the magnetite structure while Gd is attached at the nanocrystal surface, in contrast to previous results.[8, 38, 54-55]
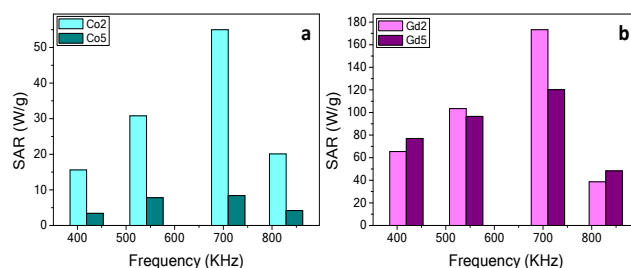

Figure 10. SAR values of aqueous dispersions of Co doped samples (a) and Gd doped samples (b) measured at 24 kA/m (419, 542 and 710 kHz) asn at 20 kA/m (829 kHz).

CONCLUSIONS

New doped magnetic nanocrystals consisting of iron oxide and other metal integrated into the structure in different ways (forming a solid solution, forming structures core/shell decorating the surface or simply nano-intermixed) have been synthesized by a simple aqueous route which can be achieved in one step. The nanostructure formed in each case is controlled by the ionic radius of the secondary metal ion and the solubility of the metal hydroxide that controls the degree of simultaneity of the precipitation of both hydroxides in the initial steps of the reaction.

22

Important points that have been concluded from this work: (1) The introduction of an extra element is successful in all cases below 5 %$_{at}$ reproducing the initial proportion of the mixture. (2) Above 5 %$_{at}$ good results have been obtained with bismuth and gold but with the appearance of a secondary phase of goethite in the last case. (3) The particle size generally decreases with doping, except for gadolinium. (4) Magnetic properties of the doped systems are not damaged by the cocrystallization of any of the metal tested below the 5 %$_{at}$ of doping. All samples present lower coercivities due to surface effects but Co that produces an enhancement of the coercivity due to their increase in magnetic anisotropy. (5) The UV absorbance of nanocrystalline gold has been observed in gold decorated magnetite nanocrystals. (6) Samples doped with Gd presents higher SAR values than samples doped with Co for the measurement conditions used. (7) Samples Co2 and Bi20 present good properties as contrast agents for MRI and CT, respectively.

ASSOCIATED CONTENT

Supporting Information. TEM micrographs, particle size distributions of Bi, Co, Gd and Au doped magnetic nanocrystals and electron diffraction of Gd5 sample. This material is available free of charge via the Internet at http://pubs.acs.org.

AUTHOR INFORMATION

Corresponding Author

* yurena.luengo@imdea.org
Notes
The authors declare no competing financial interest.

23

REFERENCES

1.   Cheon, J.; Lee, J. H. Synergistically Integrated Nanoparticles as Multimodal Probes for Nanobiotechnology. *Acc. Chem. Res.* **2008**, *41*, 1630-40.

2.   Lee, N.; Choi, S. H.; Hyeon, T. Nano-Sized Ct Contrast Agents. *Adv. Mater.* **2013**, *25*, 2641-60.

3.   Tan, R. L.; Song, X.; Chen, B.; Chong, W. H.; Fang, Y.; Zhang, H.; Wei, J.; Chen, H. Levelling the Playing Field: Screening for Synergistic Effects in Coalesced Bimetallic Nanoparticles. *Nanoscale* **2016**, *8*, 3447-53.

4.   Sun, S.; Zeng, H.; Robinson, D. B.; Raoux, S.; Rice, P. M.; Wang, S. X.; Li, G. Monodisperse MFe2o4 (M = Fe, Co, Mn) Nanoparticles. *J. Am. Chem. Soc.* **2004**, *126*, 273-9.

5.   Deepak, F. L.; Bañobre-López, M.; Carbó-Argibay, E.; Cerqueira, M. F.; Piñeiro-Redondo, Y.; Rivas, J.; Thompson, C. M.; Kamali, S.; Rodríguez-Abreu, C.; Kovnir, K.; et al. A

Systematic Study of the Structural and Magnetic Properties of Mn-, Co-, and Ni-Doped Colloidal Magnetite Nanoparticles. *J. Phys. Chem*. C **2015**, *119,* 11947-11957.

6.   Figuerola, A.; Di Corato, R.; Manna, L.; Pellegrino, T. From Iron Oxide Nanoparticles Towards Advanced Iron-Based Inorganic Materials Designed for Biomedical Applications. *Pharmacol. Res.* **2010**, *62*, 126-43.

7.   Prodi, L.; Rampazzo, E.; Rastrelli, F.; Speghini, A.; Zaccheroni, N. Imaging Agents Based on Lanthanide Doped Nanoparticles. *Chem. Soc. Rev* **2015**, *44*, 4922-52.

8.   Park, J. C.; Yeo, S.; Kim, M.; Lee, G. T.; Seo, J. H. Synthesis and Characterization of Novel Lanthanide-Doped Magnetite@Au Core@Shell Nanoparticles. *Mater. Lett.* **2016**, *181*, 272-277.

9.   Sathya, A.; Guardia, P.; Brescia, R.; Silvestri, N.; Pugliese, G.; Nitti, S.; Manna, L.; Pellegrino, T. CoxFe3–xO4 Nanocubes for Theranostic Applications: Effect of Cobalt Content and Particle Size. *Chem. Mater.* **2016**, *28*, 1769-1780.

10.   Zhou, Z.; Wei, J.; Gao, J.; Hou, F. One-Step Synthesis and Magnetic Properties of Ni-Fe3o4@Pi Core–Shell Composite Microspheres. *High Perform. Polym.* **2017**, *29*, 608-615.

11.   Casula, M. F.; Conca, E.; Bakaimi, I.; Sathya, A.; Materia, M. E.; Casu, A.; Falqui, A.; Sogne, E.; Pellegrino, T.; Kanaras, A. G. Manganese Doped-Iron Oxide Nanoparticle Clusters and Their Potential as Agents for Magnetic Resonance Imaging and Hyperthermia. *Phys. Chem. Chem. Phys*. **2016**, *18*, 16848-16855.

12.   Wang, G.; Peng, Q.; Li, Y. Lanthanide-Doped Nanocrystals: Synthesis, Optical-Magnetic Properties, and Applications. *Acc. Chem. Res*. **2011**, *44*, 322-32.

25

13. Park, J. C.; Lee, G. T.; Kim, H.-K.; Sung, B.; Lee, Y.; Kim, M.; Chang, Y.; Seo, J. H. Surface Design of Eu-Doped Iron Oxide Nanoparticles for Tuning the Magnetic Relaxivity. *ACS Appl. Mater. Interfaces* **2018**, *10*, 25080-25089.

14. Petran, A.; Radu, T.; Borodi, G.; Nan, A.; Suciu, M.; Turcu, R. Effects of Rare Earth Doping on Multi-Core Iron Oxide Nanoparticles Properties. *Appl. Surf. Sci.* **2018**, *428*, 492-499.

15. Jain, R.; Luthra, V.; Gokhale, S. Dysprosium Doping Induced Shape and Magnetic Anisotropy of Fe3−Xdyxo4 (X=0.01–0.1) Nanoparticles. *J. Magn. Magn. Mater.* **2016**, *414*, 111-115.

16. Zhang, H.; Malik, V.; Mallapragada, S.; Akinc, M. Synthesis and Characterization of Gd-Doped Magnetite Nanoparticles. *J. Magn. Magn. Mater.* **2017**, *423*, 386-394.

17. Schultz-Sikma, E. A.; Joshi, H. M.; Ma, Q.; Macrenaris, K. W.; Eckermann, A. L.; Dravid, V. P.; Meade, T. J. Probing the Chemical Stability of Mixed Ferrites: Implications for Mr Contrast Agent Design. *Chem. Mater.* **2011**, *23*, 2657-2664.

18. Sytnyk, M.; Kirchschlager, R.; Bodnarchuk, M. I.; Primetzhofer, D.; Kriegner, D.; Enser, H.; Stangl, J.; Bauer, P.; Voith, M.; Hassel, A. W.; et al. Tuning the Magnetic Properties of Metal Oxide Nanocrystal Heterostructures by Cation Exchange. *Nano Lett.* **2013**, *13*, 586-93.

19. Grigorova, M.; Blythe, H.; Blaskov, V.; Rusanov, V.; Petkov, V.; Masheva, V.; Nihtianova, D.; Martinez, L. M.; Munoz, J.; Mikhov, M. Magnetic Properties and Mössbauer Spectra of Nanosized CoFe2O4 Powders. *J. Magn. Magn. Mater.* **1998**, *183*, 163-172.

26

20. Cui, L.; Guo, P.; Zhang, G.; Li, Q.; Wang, R.; Zhou, M.; Ran, L.; Zhao, X. S. Facile Synthesis of Cobalt Ferrite Submicrospheres with Tunable Magnetic and Electrocatalytic Properties. *Colloids Surf. A* **2013**, *423*, 170-177.

21. Lopes-Moriyama, A. L.; Madigou, V.; Souza, C. P. d.; Leroux, C. Controlled Synthesis of CoFe2O4 Nano-Octahedra. *Powder Technol.* **2014**, *256*, 482-489.

22. Kumbhar, V. S.; Jagadale, A. D.; Shinde, N. M.; Lokhande, C. D. Chemical Synthesis of Spinel Cobalt Ferrite (CoFe2O4) Nano-Flakes for Supercapacitor Application. *Appl. Surf. Sci.* **2012**, *259*, 39-43.

23. Avazpour, L.; Zandi khajeh, M. A.; Toroghinejad, M. R.; Shokrollahi, H. Synthesis of Single-Phase Cobalt Ferrite Nanoparticles Via a Novel Edta/Eg Precursor-Based Route and Their Magnetic Properties. *J. Alloys Compd.* **2015**, *637*, 497-503.

24. Houshiar, M.; Zebhi, F.; Razi, Z. J.; Alidoust, A.; Askari, Z. Synthesis of Cobalt Ferrite (CoFe2O4) Nanoparticles Using Combustion, Coprecipitation, and Precipitation Methods: A Comparison Study of Size, Structural, and Magnetic Properties. *J. Magn. Magn. Mater.* **2014**, *371*, 43-48.

25. Caravan, P.; Ellison, J. J.; McMurry, T. J.; Lauffer, R. B. Gadolinium(III) Chelates as MRI Contrast Agents: Structure, Dynamics, and Applications. *Chem. Rev.* **1999**, *99*, 2293-2352.

26. Bottrill, M.; Kwok, L.; Long, N. J. Lanthanides in Magnetic Resonance Imaging. *Chem. Soc. Rev.* **2006**, *35*, 557-71.

27

27.   Bae, K. H.; Kim, Y. B.; Lee, Y.; Hwang, J.; Park, H.; Park, T. G. Bioinspired Synthesis and Characterization of Gadolinium-Labeled Magnetite Nanoparticles for Dual Contrast T1- and T2-Weighted Magnetic Resonance Imaging. *Bioconjug. Chem.* **2010**, *21*, 505-12.

28.   Choi, J. S.; Lee, J. H.; Shin, T. H.; Song, H. T.; Kim, E. Y.; Cheon, J. Self-Confirming "and" Logic Nanoparticles for Fault-Free MRI. *J. Am. Chem. Soc.* **2010**, *132*, 11015-7.

29.   Zhou, Z.; Huang, D.; Bao, J.; Chen, Q.; Liu, G.; Chen, Z.; Chen, X.; Gao, J. A Synergistically Enhanced T(1) -T(2) Dual-Modal Contrast Agent. *Adv. Mater.* **2012**, *24*, 6223-8.

30.   Xiao, N.; Gu, W.; Wang, H.; Deng, Y.; Shi, X.; Ye, L. T1-T2 Dual-Modal MRI of Brain Gliomas Using Pegylated Gd-Doped Iron Oxide Nanoparticles. *J. Colloid Interface Sci.* **2014**, *417*, 159-65.

31.   Wang, X.; Zhou, Z.; Wang, Z.; Xue, Y.; Zeng, Y.; Gao, J.; Zhu, L.; Zhang, X.; Liu, G.; Chen, X. Gadolinium Embedded Iron Oxide Nanoclusters as T1-T2 Dual-Modal MRI-Visible Vectors for Safe and Efficient Sirna Delivery. *Nanoscale* **2013**, *5*, 8098-104.

32.   Zhou, Z.; Wang, L.; Chi, X.; Bao, J.; Yang, L.; Zhao, W.; Chen, Z.; Wang, X.; Chen, X.; Gao, J. Engineered Iron-Oxide-Based Nanoparticles as Enhanced T1 Contrast Agents for Efficient Tumor Imaging. *ACS Nano* **2013**, *7*, 3287-96.

33.   Shin, T. H.; Choi, Y.; Kim, S.; Cheon, J. Recent Advances in Magnetic Nanoparticle-Based Multi-Modal Imaging. *Chem. Soc. Rev.* **2015**, *44*, 4501-16.

34.   Sieber, M. A.; Steger-Hartmann, T.; Lengsfeld, P.; Pietsch, H. Gadolinium-Based Contrast Agents and Nsf: Evidence from Animal Experience. *J. Magn. Reson. Imaging* **2009**, *30*, 1268-1276.

28

35. Lee, N.; Hyeon, T. Designed Synthesis of Uniformly Sized Iron Oxide Nanoparticles for Efficient Magnetic Resonance Imaging Contrast Agents. *Chem. Soc. Rev.* **2012**, *41*, 2575-2589.

36. Groult, H.; Ruiz-Cabello, J.; Lechuga-Vieco, A. V.; Mateo, J.; Benito, M.; Bilbao, I.; Martinez-Alcazar, M. P.; Lopez, J. A.; Vazquez, J.; Herranz, F. F. Phosphatidylcholine-Coated Iron Oxide Nanomicelles for in Vivo Prolonged Circulation Time with an Antibiofouling Protein Corona. *Chem. Eur. J.* **2014**, *20*, 16662-16671.

37. Drake, P.; Cho, H.-J.; Shih, P.-S.; Kao, C.-H.; Lee, K.-F.; Kuo, C.-H.; Lin, X.-Z.; Lin, Y.-J. Gd-Doped Iron-Oxide Nanoparticles for Tumour Therapy Via Magnetic Field Hyperthermia. *J. Mater. Chem.* **2007**, *17*, 4914.

38. Douglas, F. J.; MacLaren, D. A.; Maclean, N.; Andreu, I.; Kettles, F. J.; Tuna, F.; Berry, C. C.; Castro, M.; Murrie, M. Gadolinium-Doped Magnetite Nanoparticles from a Single-Source Precursor. *RSC Adv.* **2016**, *6*, 74500-74505.

39. Andrés-Vergés, M.; del Puerto Morales, M.; Veintemillas-Verdaguer, S.; Palomares, F. J.; Serna, C. J. Core/Shell Magnetite/Bismuth Oxide Nanocrystals with Tunable Size, Colloidal, and Magnetic Properties. *Chem. Mater.* **2012**, *24*, 319-324.

40. Laguna-Marco, M. A.; Piquer, C.; Roca, A. G.; Boada, R.; Andres-Verges, M.; Veintemillas-Verdaguer, S.; Serna, C. J.; Iadecola, A.; Chaboy, J. Structural Determination of Bi-Doped Magnetite Multifunctional Nanoparticles for Contrast Imaging. *Phys. Chem. Chem. Phys.* **2014**, *16*, 18301-10.

29

41. Veintemillas-Verdaguer, S.; Luengo, Y.; Serna, C. J.; Andres-Verges, M.; Varela, M.; Calero, M.; Lazaro-Carrillo, A.; Villanueva, A.; Sisniega, A.; Montesinos, P.; et al. Bismuth Labeling for the CT Assessment of Local Administration of Magnetic Nanoparticles. *Nanotechnology* **2015**, *26*, 135101.

42. Shah, B.; Yin, P. T.; Ghoshal, S.; Lee, K. B. Multimodal Magnetic Core-Shell Nanoparticles for Effective Stem-Cell Differentiation and Imaging. *Angew. Chem. Int. Ed. Engl.* **2013**, *52*, 6190-5.

43. Pissuwan, D.; Valenzuela, S. M.; Cortie, M. B. Therapeutic Possibilities of Plasmonically Heated Gold Nanoparticles. *Trends Biotechnol.* **2006**, *24*, 62-7.

44. Hirsch, L. R.; Stafford, R. J.; Bankson, J. A.; Sershen, S. R.; Rivera, B.; Price, R. E.; Hazle, J. D.; Halas, N. J.; West, J. L. Nanoshell-Mediated near-Infrared Thermal Therapy of Tumors under Magnetic Resonance Guidance. *Proc. Natl. Acad. Sci. U S A* **2003**, *100*, 13549-54.

45. Ke, H.; Wang, J.; Dai, Z.; Jin, Y.; Qu, E.; Xing, Z.; Guo, C.; Yue, X.; Liu, J. Gold-Nanoshelled Microcapsules: A Theranostic Agent for Ultrasound Contrast Imaging and Photothermal Therapy. *Angew. Chem. Int. Ed. Engl.* **2011**, *50*, 3017-21.

46. Caruntu, D.; Cushing, B. L.; Caruntu, G.; O'Connor, C. J. Attachment of Gold Nanograins Onto Colloidal Magnetite Nanocrystals. *Chem. Mater.* **2005**, *17*, 3398-3402.

47. Bao, J.; Chen, W.; Liu, T.; Zhu, Y.; Jin, P.; Wang, L.; Liu, J.; Wei, Y.; Li, Y. Bifunctional Au-Fe3O4 Nanoparticles for Protein Separation. *ACS Nano* **2007**, *1*, 293-8.

30

48.   Andrés-Vergés, M.; Costo, R.; Roca, A. G.; Marco, J. F.; Goya, G. F.; Serna, C. J.; Morales, M. P. Uniform and Water Stable Magnetite Nanoparticles with Diameters around the Monodomain–Multidomain Limit. *J. Phys. D Appl. Phys.* **2008**, *41*, 134003.

49.   Li, Y.; Li, C. H.; Talham, D. R. One-Step Synthesis of Gradient Gadolinium Ironhexacyanoferrate Nanoparticles: A New Particle Design Easily Combining Mri Contrast and Photothermal Therapy. *Nanoscale* **2015**, *7*, 5209-16.

50.   Lide, D. R. *Crc Handbook of Chemistry and Physics : A Ready-Reference Book of Chemical and Physical Data*; CRC Press: Boca Raton [etc.], 1992.

51.   Rodenas, L. G.; Liberman, S. J. Hydrolysis of Gadolinium(III) in Light and Heavy Water. *Talanta* **1991**, *38*, 313-318.

52.   Tamura, H.; Matijevic, E. Precipitation of Cobalt Ferrites. *J. Colloid Interface Sci.* **1982**, *90*, 100-109.

53.   Takeno, N. *Atlas of Eh-Ph Diagrams: Intercomparison of Thermodynamics Databases* Research Center for Deep Geological Environments: 2005.

54.   Nikoforov, V. N.; Oksengendler, B. L. Magnetometric Study of Gadolinium Solubility in Magnetite Nanocrystals. *Inorg. Mater.* **2014**, *50*, 1222-1225.

55.   Orbaek, A. W.; Morrow, L.; Maguire-Boyle, S. J.; Barron, A. R. Reagent Control Over the Composition of Mixed Metal Oxide Nanoparticles. *J. Exp. Nanosci.* **2013**, *10*, 324-349.

31

56. Lyon, J. L.; Fleming, D. A.; Stone, M. B.; Schiffer, P.; Williams, M. E. Synthesis of Fe Oxide Core/Au Shell Nanoparticles by Iterative Hydroxylamine Seeding. *Nano Lett.* **2004**, *4*, 719-723.

57. Goon, I. Y.; Lai, L. M. H.; Lim, M.; Munroe, P.; Gooding, J. J.; Amal, R. Fabrication and Dispersion of Gold-Shell-Protected Magnetite Nanoparticles: Systematic Control Using Polyethyleneimine. *ChemMater.* **2009**, *21*, 673-681.

58. Cornell, R. M.; Schwertmann, U. *The Iron Oxides: Structure, Properties, Reactions, Occurrences and Uses*; Wiley, 2006.

59. Fantechi, E.; Innocenti, C.; Albino, M.; Lottini, E.; Sangregorio, C. Influence of Cobalt Doping on the Hyperthermic Efficiency of Magnetite Nanoparticles. *J. Magn. Magn. Mater.* **2015**, *380*, 365-371.

60. Yu, Y.; Mendoza-Garcia, A.; Ning, B.; Sun, S. Cobalt-Substituted Magnetite Nanoparticles and Their Assembly into Ferrimagnetic Nanoparticle Arrays. *Adv. Mater.* **2013**, *25*, 3090-4.

61. Taboada, E.; Rodriguez, E.; Roig, A.; Oro, J.; Roch, A.; Muller, R. N. Relaxometric and Magnetic Characterization of Ultrasmall Iron Oxide Nanoparticles with High Magnetization. Evaluation as Potential T1 Magnetic Resonance Imaging Contrast Agents for Molecular Imaging. *Langmuir* **2007**, *23*, 4583-8.

62. Roca, A. G.; Veintemillas-Verdaguer, S.; Port, M.; Robic, C.; Serna, C. J.; Morales, M. P. Effect of Nanoparticle and Aggregate Size on the Relaxometric Properties of Mr Contrast Agents Based on High Quality Magnetite Nanoparticles. *J. Phys. Chem. B* **2009**, *113*, 7033-9.

32

63.   Sun, L.; Zang, Y.; Sun, M.; Wang, H.; Zhu, X.; Xu, S.; Yang, Q.; Li, Y.; Shan, Y. Synthesis of Magnetic and Fluorescent Multifunctional Hollow Silica Nanocomposites for Live Cell Imaging. *J. Colloid Interface Sci.* **2010**, *350*, 90-8.

64.   Di Corato, R.; Espinosa, A.; Lartigue, L.; Tharaud, M.; Chat, S.; Pellegrino, T.; Menager, C.; Gazeau, F.; Wilhelm, C. Magnetic Hyperthermia Efficiency in the Cellular Environment for Different Nanoparticle Designs. *Biomaterials* **2014**, *35*, 6400-11.

33

TOC Graphic